ACS APPLIED ENERGY MATERIALS

www.acsaem.org Article

Deciphering the Exceptional Performance of NiFe Hydroxide for the Oxygen Evolution Reaction in an Anion Exchange Membrane Electrolyzer

Li Wang,* Viktoriia A. Saveleva, Mohammad J. Eslamibidgoli, Denis Antipin, Corinne Bouillet, Indro Biswas, Aldo S. Gago, Seyed S. Hosseiny, Pawel Gazdzicki, Michael H. Eikerling, Elena R. Savinova, and K. Andreas Friedrich

Cite This: https://doi.org/10.1021/acsaem.1c03761 Read Online

ACCESS | Metrics & More | Article Recommendations | Supporting Information

ABSTRACT: Hydrogen production *via* water electrolysis with renewable electricity as input will be crucial for the coming defossilized energy age. Herein, we report an anion exchange membrane electrolyzer using Fe-doped Ni hydroxide as an anode catalyst that is on par with proton exchange membrane electrolyzers in terms of the performance, 2 A cm^{-2} at 2.046 V and 50 °C. We found that Fe doping stabilizes the α-$Ni(OH)_2$ phase, which is key to ensure the fast $Ni(OH)_2$/NiOOH redox transition and the subsequent fast reaction between $Ni^{3+/4+}$ and the electrolyte (OH^-), resulting in the excellent oxygen evolution reaction activity of Fe-doped Ni hydroxide. Spin-polarized DFT + *U* computations reveal that the local arrangement of Fe^{3+} with $Ni^{3+/4+}$ plays a crucial role in enabling the high OER activity on the (001) facet of this anode catalyst.

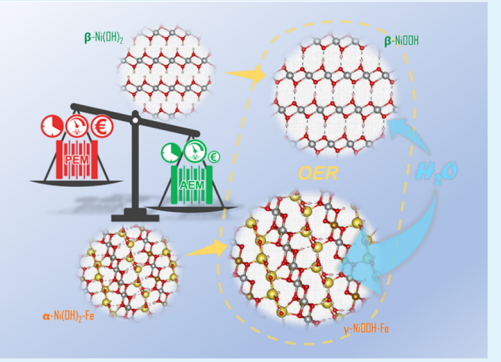

KEYWORDS: *AEM electrolysis, Fe-doped Ni hydroxide, OER activity, fast kinetics, stabilization of α-$Ni(OH)_2$ phase, DFT + U computation*

1. INTRODUCTION

Rising awareness of the adverse impacts of climate change is accelerating efforts toward a defossilized and renewable energy infrastructure. In this context, different scenarios are considered to meet ambitious targets for the reduction and elimination of CO_2 emissions. Hydrogen will be indispensable as a carrier and storage medium for renewably generated electricity, and it will have to be produced in large amounts through water electrolysis. Proton exchange membrane (PEM) electrolyzers could provide sufficient performance and durability, but their deployment at the required scale fails because of the scarcity of platinum group metals (PGM) that they need as electrocatalysts.[1,2] Conventional alkaline electrolyzers (AEL), on the other hand, are lacking in operational flexibility hindering both from multimegawatt scale installation at a low cost.

Recently, the development of anion exchange membrane (AEM) electrolyzers that could combine advantages of both PEM and AEL systems has gained significant traction.[3] Vincent et al.[4,5] evaluated different AEMs and studied the effect of adding different supporting electrolytes ($KHCO_3$, K_2CO_3, and KOH). The best performance was achieved for 500 mA cm^{-2} and 1.95 V at 60 °C with 1% K_2CO_3 electrolyte when using the Tokuyama A201 membrane, $CuCoO_x$, and Ni/(CeO_2-La_2O_3)/C as anode and cathode catalyst, respectively. Chen et al.[6] demonstrated the possibility of achieving 1.0 A cm^{-2} at 1.57 V and 80 °C in an AEM electrolyzer when NH_3/H_2-treated and subsequently anodically oxidized Fe-NiMo was employed as an anode catalyst. With a feed of deionized (DI) water, Fabbri et al.[7] reported a high cell performance at 200 mA cm^{-2} using a flame-sprayed $Ba_{0.5}Sr_{0.5}Co_{0.8}Fe_{0.2}O_{3-\delta}$ anode catalyst as opposed to commercial IrO_2. More recently, Li et al.[8] showed the effect of electrode binders on the cell performance, using a quaternized polystyrene electrode binder and PtRu as a cathode catalyst, and reported a high current density of 2.7 A cm^{-2} at 1.8 V and 85 °C, but durability remains a challenge. In spite of significant progresses recently made, AEM electrolyzers need further advances in terms of performance and longevity to achieve readiness for a megawatt-scale deployment. This requires selection, design, and optimization of component materials, electrode structure and composition, membrane structure and properties, as well as furthering the

Received: November 30, 2021
Accepted: January 3, 2022

understanding of the electrocatalytic processes on those platinum group metal (PGM)-free anode and cathode catalysts.

The anode catalyst is of utmost importance in this context, as the oxygen evolution reaction (OER) accounts for the major proportion of irreversible voltage losses in the AEM cell.[9] Fe-doped Ni oxyhydroxide is one of the best-performing PGM-free OER catalysts under such conditions.[10] It has long been known that Fe incorporation into Ni-based OER electrocatalysts, either intentionally *via* doping or incidentally as an impurity, can dramatically increase their OER activity.[11,12] However, the modifications in the surface electronic structure and the reaction mechanism as a result of Fe incorporation that are deemed responsible for the observed activity have remained elusive and controversial.[12−20]

In this work, we fabricated an AEM electrolyzer with an in-house made Fe-doped $Ni(OH)_2$ precursor phase (denoted as $Ni(OH)_2$-Fe), which, under anodic polarization, transforms into a highly active Fe-doped NiOOH anode catalyst (denoted as NiOOH-Fe). In terms of activity and performance stability, our electrolyzer has demonstrated promising progress toward PEM-based systems. The cell was operated at a constant current density of 1 A cm^{-2} and 50 °C for around 500 h without noticeable degradation, indicating a promising step toward industrial requirements. We have used pure $Ni(OH)_2$ as a benchmark for quantifying the activity enhancement upon doping with Fe. On top of that, efforts were made to untangle the high OER activity of $Ni(OH)_2$-Fe using various characterization methods and DFT + *U* computations. Through various *ex situ* and *in situ* characterization methods, theoretical calculations, together with the validation of $Ni(OH)_2$-Fe in a technical AEM electrolyzer reactor, this study provides a comprehensive approach toward understanding Ni(Fe)-based oxyhydroxide as an OER electrocatalyst, suitable for use in the AEM electrolysis technology.

2. EXPERIMENTAL SECTION

2.1. Material Preparation. Both catalysts $Ni(OH)_2$ and $Ni(OH)_2$-Fe are prepared *via* an electrodissolution−precipitation approach, similar to the one reported by Jung and co-workers.[21] In an electrochemical cell, a metal wire was taken as the anode, NiFe wire (NiFe 70/30 alloy wire, diameter 0.9 mm, Scott Precision Wire) for $Ni(OH)_2$-Fe, and Ni wire (Goodfellow metals, diameter 0.5 mm, purity > 99.99%) was used for $Ni(OH)_2$. Pt foil (6.28 cm^2) was used as the cathode, and the electrolyte was 0.03 M NaCl (Merck, purity ≥ 99.5%; Fe impurities ≤ 0.0001%) solution. To avoid the Fe contamination for $Ni(OH)_2$ to our best possible extent, high-purity Ni wire and NaCl salt, as well as ultrapure water, were used for the synthesis. For both catalysts, the dissolution of metal wires and subsequent precipitation were driven by a Metrohm Autolab PGSTAT302N potentiostat under galvanostatic mode with a current density of 0.1 mA cm^{-2}; meanwhile, the NaCl electrolyte was stirred with a magnetic stirrer bar at 200 rpm. The dissolution−precipitation time for each sample lasts 80 h, and the precipitates were rinsed using plenty of ultrapure water and finally collected by centrifugation, and then dried at 60 °C in air overnight.

2.2. Physical Characterization. *2.2.1. X-ray Powder Diffraction (XRD).* Both $Ni(OH)_2$-Fe and $Ni(OH)_2$ powders were characterized by X-ray diffraction (D8 Discover GADDS diffractometer equipped with a VÅNTEC-2000 areal detector). The measurements were carried out in reflection mode in four frames with $\theta_1 = \theta_2$ (180 s per frame, starting with $\theta = 12°$) and a step size of $2\theta = 23°$ by applying a tuned monochromatic and parallel X-ray beam (Cu Kα). The accelerating voltage and tube current were 45 kV and 0.650 mA, respectively.

2.2.2. Ultrahigh-Vacuum X-ray Photoelectron Spectroscopy (UHV-XPS). $Ni(OH)_2$-Fe and $Ni(OH)_2$ powder samples were placed between two Au foils and pressed at ∼50 MPa into a pellet. The pellet, attached to one of the Au foils, was mounted on the XPS sample holder and transferred into the UHV system (Thermo Scientific ESCALAB 250) with a base pressure of 1×10^{-9} mbar. The samples were exposed to nonmonochromated Al Kα X-ray radiation (Thermo Scientific XR4, 300 W). The lenses of the hemispherical electron energy analyzer were set to analyze an area of 0.8 mm^2. Spectra were energy-calibrated with reference to the Ag $3d_{3/2}$ signal of a clean etched silver surface. The signal deconvolution and quantification were carried out using Unifit 2016 and tabled atomic photoionization cross sections.[22,23] A pure NiO reference (Sigma-Aldrich) was investigated in the same manner.

2.2.3. Scanning Electron Microscopy (SEM). SEM analyses of both $Ni(OH)_2$-Fe and $Ni(OH)_2$ were performed by employing a Zeiss ULTRA plus microscope with Charge Compensation. Secondary electrons were collected to probe their morphologies, the accelerating voltage was 2 kV for $Ni(OH)_2$-Fe and 3 kV for $Ni(OH)_2$.

2.2.4. Scanning Transmission Electron Microscopy (STEM). STEM imaging and EDX mapping were performed using a JEOL2100F, Cs-corrected microscope at the probe level and operating at 100 kV. The resolution in STEM imaging was 0.15 nm. The EDX mapping was acquired thanks to an SDD Jeol detector, with a detection surface of 60 mm^2 and with a 0.2 nm spatial resolution.

2.2.5. Thermogravimetric Analysis (TGA). Both $Ni(OH)_2$-Fe and $Ni(OH)_2$ samples were characterized by thermogravimetric analysis (TGA, Netzsch Jupiter 449C) in flowing Ar atmosphere (30 mL min^{-1}) with a heating ramp rate of 5 °C from 30 °C to 1200 °C; at the same time, thermogravimetric and differential scanning calorimetric (DSC) data were recorded.

2.3. Rotating Disk Electrode (RDE) Measurements. Cyclic voltammetry and scan rate dependence of the redox peaks were conducted in a standard three-electrode cell at 25 °C. All parts of the cell that were in contact with the electrolyte were made from PTFE, and all remaining parts were made from Pyrex glass. Pt wire and Hg/HgO/0.1 M NaOH were used as the counter electrode and the reference electrode, respectively. The electrode potential was converted to the RHE scale.

Glassy carbon RDE with 5 mm diameter coated with a catalytic ink was used as the working electrode. GC was polished with alumina paste (down to 0.05 μm) prior to each measurement.

The catalytic ink was prepared by the following procedure: calculated amounts of powder (either $Ni(OH)_2$-Fe or $Ni(OH)_2$) and Sibunit Carbon were mixed and ground together with a 1:1 oxide/carbon ratio. Then, a required amount of ultrapure water was added and the mixture was ultrasonicated for 30 min. Prepared ink was drop-cast onto the surface of GC three times to obtain 15 $\mu g\ cm_{geo}^{-2}$ hydroxide loading. After the layer was dried, 2 μL of OH^--modified dilute Nafion solution[24] was added on top to provide the ionomer loading of ca. 1.3 $\mu g\ cm^{-2}$.

Electrochemical measurements were performed using an AutoLab PGSTAT302N potentiostat equipped with an analog scan generator. N_2-saturated 0.1 M NaOH was used as the electrolyte. Electrolyte resistance between WE and RE was determined with EIS (measured in the 1−100 000 Hz range). The obtained value of 33 Ω was used for the *iR* correction. The rotating speed was set to 1600 rpm to remove O_2 bubbles from the surface of the WE. First, 5 CV scans in a wide range from 0.9 to 1.6 V vs RHE were performed to identify the voltage range with redox peaks (i.e., 1.2−1.5 V vs RHE) and stabilize the electrode. Second, the voltage range was set to 1.2−1.5 V vs RHE and four consecutive CV scans were recorded for each scan rate (from 5 up to 1000 mV s^{-1}). The fourth scan for each scan rate is plotted in Figure 2B,C.

2.4. Cell Measurements. The cell measurements were conducted in a homemade AEM electrolyzer with an active area of 4 cm^2. Both bipolar plates (BPP) are made of stainless steel (316L) without flow field. On both anode and cathode, it comprises two gas diffusion layers (GDL): the stainless steel gradient porous metal framework

https://doi.org/10.1021/acsaem.1c03761
ACS Appl. Energy Mater. XXXX, XXX, XXX−XXX

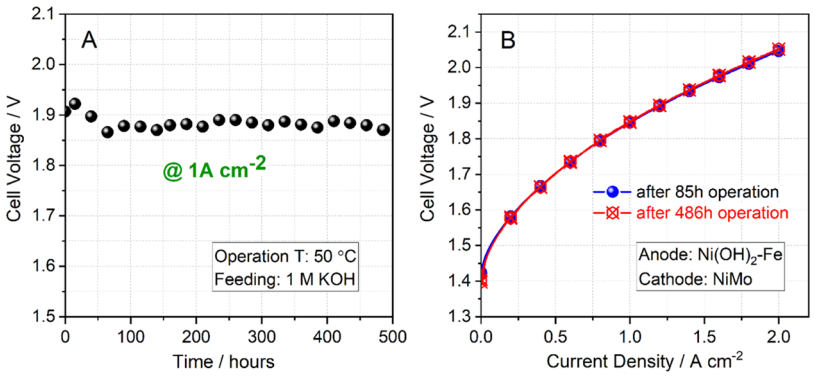

Figure 1. Cell performance with long-term performance stability (A) and current−voltage (i−V) curves after different operation times (B) of an AEM electrolyzer using $Ni(OH)_2$-Fe and NiMo as the anode and cathode catalyst, respectively; operation temperature: 50 °C; feedstock: 1 M KOH.

(GPMF, 4.25 mm thickness and 1.199 ± 0.002 g cm^2 area specific weight, MeliCon GmbH, Germany) is served as the first GDL, and closely attached to BPP, the second GDL is previously rolled Ni foam (thickness 0.5 mm) which is placed between the dense side of GPMF and membrane. The AEM used in the tests is Tokuyama A201 membrane (thickness in dry form: 28 μm; Tokuyama Corporation, Japan). The ion exchange capacity (IEC) for A201 membrane is 1.8 mmol g^{-1}, the water uptake is 30%, and the ion conductivity in HCO_3^- form is 12 mS cm^{-1}.[25] $Ni(OH)_2$-Fe synthesized in this work was taken as the anode catalyst with a loading of 4 mg cm^{-2}, while Raney NiMo with a loading of 25.2 mg cm^{-2} was used as the cathode catalyst that is *in situ* formed from NiAlMo powder (Ni-Al-Mo: 39/44/17; grain size: ∼45 μm; H.C. Starck GmbH, Germany). On both cathodic and anodic catalytic layers, multiwall carbon nanotubes (CNTs, BAYTUBES C 70 P, Bayer MaterialScience AG) were added as additives to enhance the electroconductivity, and the loading is 6 mg cm^{-2} for both sides. The ionomer used for the measurements is Sustainion XA-9 Alkaline Ionomer (5% in ethanol, Dioxide Materials), and the ionomer ratios for cathode and anode are 17% and 30%, respectively. The electrodes were prepared *via* the catalyst-coated substrate (CCS) approach, and the blended inks were coated on the above-mentioned second GDL—Ni foam—and dried at 60 °C in air overnight. Hot press was not applied on forming the electrode membrane assembly (MEA).

Once assembled, the cell was mounted onto a house-built electrolyzer test station, which was controlled by LabView software. First, the cell was activated at room temperature with a current density of 25 mA cm^{-2} for 24 h, followed by a second phase activation with an increased current density of 100 mA cm^{-2} for another 12 h. Afterwards, the cell temperature was increased to 50 °C and the current density was increased to 1 A cm^{-2} for constant operation. The entire test was uninterrupted except that the current−voltage (i−V) curves were measured after 85 h operation and at the end of the test (486 h). During the durability test, the feeding stock 1 M KOH was completely replaced with freshly prepared solution every 72 h.

2.5. DFT + *U* Computations. Spin-polarized DFT + U calculations were performed with VASP.[26,27] The ionic cores were represented by projector augmented waves (PAW).[28] Kohn−Sham one-electron wave functions were expanded in a plane-wave basis set with an energy cutoff of 500 eV. Electronic exchange and correlation effects were incorporated within the generalized gradient approximation (GGA), using the PBE exchange−correlation functional.[29] The DFT + U method has been employed to account for the strong correlations of d-electrons of Ni and Fe atoms. We used the approach by Dudarev et al.[30] with effective Hubbard U_{eff} parameters (U−J) of 5.5 and 3.3 eV for Ni and Fe, respectively, which was calculated using linear response theory[31] by Li and Selloni.[32] A geometry relaxation for bulk NiOOH was performed with a 6 × 6 × 2 Monkhorst−Pack k-point mesh[33] and a force threshold of 0.05 eV $Å^{-1}$. For geometry optimizations of the extended surface models, we used 4 × 4 × 1 k-points. Additional computation details are given in the Supporting Information.

3. RESULTS AND DISCUSSION

To target a low-cost water electrolyzer, all components consist of PGM-free materials. Highly porous Raney NiMo formed from NiAlMo powder is used as a cathode catalyst. Tokuyama A201 with a thickness of 28 μm is employed as the membrane. $Ni(OH)_2$-Fe nanopowder is used as the anode catalyst. It was synthesized *via* electrochemical dissolution−precipitation and possesses a flake-like morphology. In this study, 30 wt.% Fe dopant was selected to have the highest OER activity.[12,19] The other parts at anode and cathode are identical, Ni foam serves as the current collector, GPMF made of stainless steel (SS) as a gas diffusion layer, and an SS plate without flow channel was used as BPP. Once the AEM cell was assembled, an activation procedure (see the SI) was carried out to form the Raney NiMo cathode. Subsequently, the cell was set to 1 A cm^{-2} at 50 °C and constantly operated for 486 h, feeding 1 M KOH solution to both anode and cathode. The performance stability is shown in Figure 1A, where cell voltage is plotted versus operation time. The cell voltage did not exhibit any noticeable increase during the duration of this test. The current−voltage (i−V) curves shown in Figure 1B were measured up to 2 A cm^{-2} after 85 hrs operation and at the end of the test (486 hrs). First, the overlapped i−V curves together with the stable cell voltage *vs* time reveal the high-performance stability of the configured cell, demonstrating its capability for long-term operation at 1 A cm^{-2}.[9] Second, the achieved cell performance is close to the performance of state-of-the-art PEM demonstrators.[9,34] Using the NiFe anode and the NiFeCo cathode in the AEM electrolysis concept, Kaczur et al. achieved a cell voltage of 1.9 V at 1 A cm^{-2} and 60 °C.[35] Koshikawa et al. also reported an AEM electrolysis cell test using NiFe-LDH/KB anode; an excellent cell voltage of 1.59 V was recorded at 1 A cm^{-2}, but the cathode contained Pt/C catalyst with 1.3 mg cm^{-2} loading and the cell was operated at 80 °C.[36] It is worth noting that during the first 80 hrs, the cell voltage experienced a slight increase followed by a gradual decrease until it reached a stable value. This observation might be attributed to a breaking-in period of the cell as well as to the cathode aging effect because of the dissolution of residual molybdenum not incorporated into an alloy phase in the Raney NiMo electrocatalyst,[37] whereas the NiOOH-Fe OER catalyst is considered structure-stable as a function of time.[12] However, regarding the lifetime-performance assessment, one

https://doi.org/10.1021/acsaem.1c03761
ACS Appl. Energy Mater. XXXX, XXX, XXX−XXX

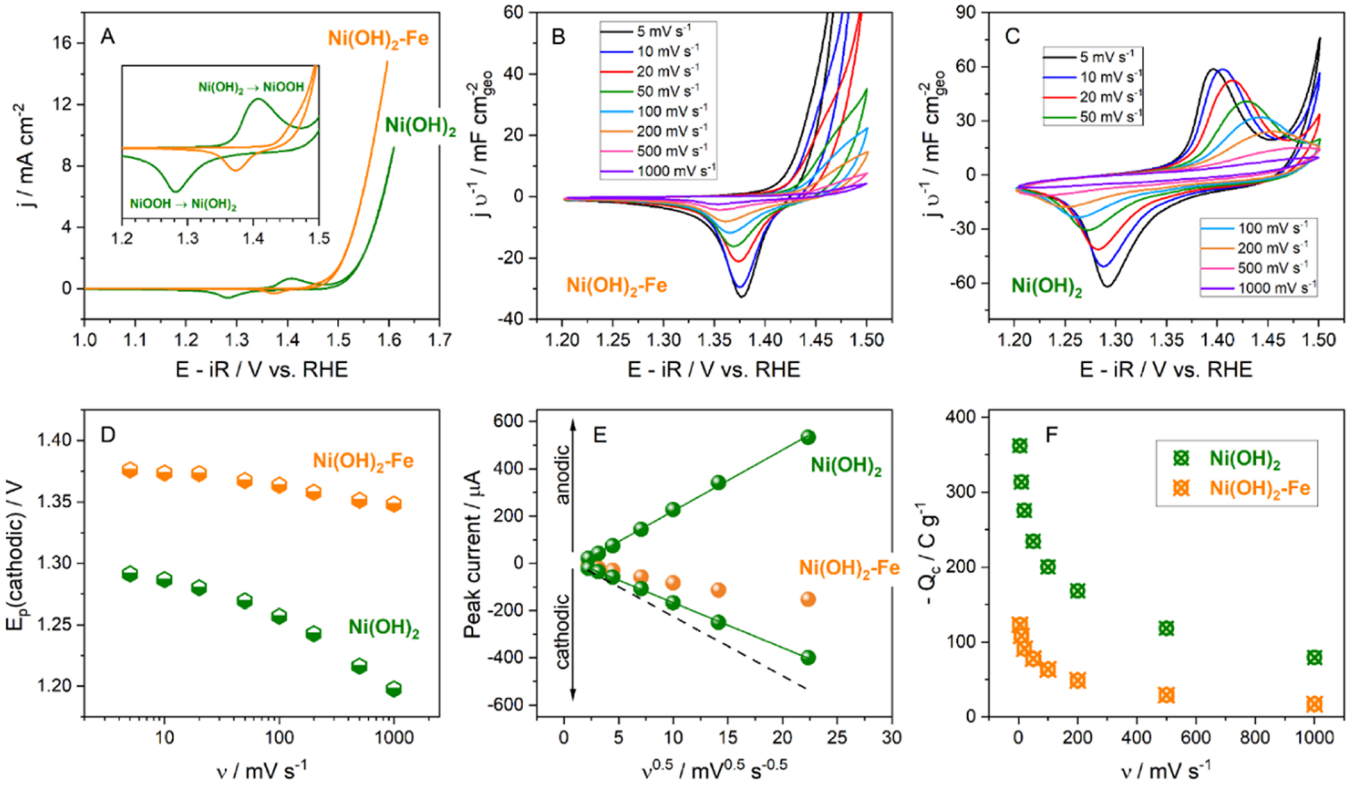

Figure 2. Electrochemical characterization using rotating disk electrode: (A) CVs for $Ni(OH)_2$-Fe and $Ni(OH)_2$ in 0.1 M NaOH at 10 mV s^{-1}; scan rate dependence of the $Ni(OH)_2$/NiOOH redox peaks of (B) $Ni(OH)_2$-Fe and (C) $Ni(OH)_2$ (current is normalized to the scan rate); (D) cathodic peak potential position (NiOOH → $Ni(OH)_2$ transition) as a function of the scan rate for both samples; (E) scan rate dependence of the peak currents; and (F) charge of the cathodic peak as a function of the scan rate for $Ni(OH)_2$-Fe and $Ni(OH)_2$. Catalyst loading: 15 μg cm^{-2}.

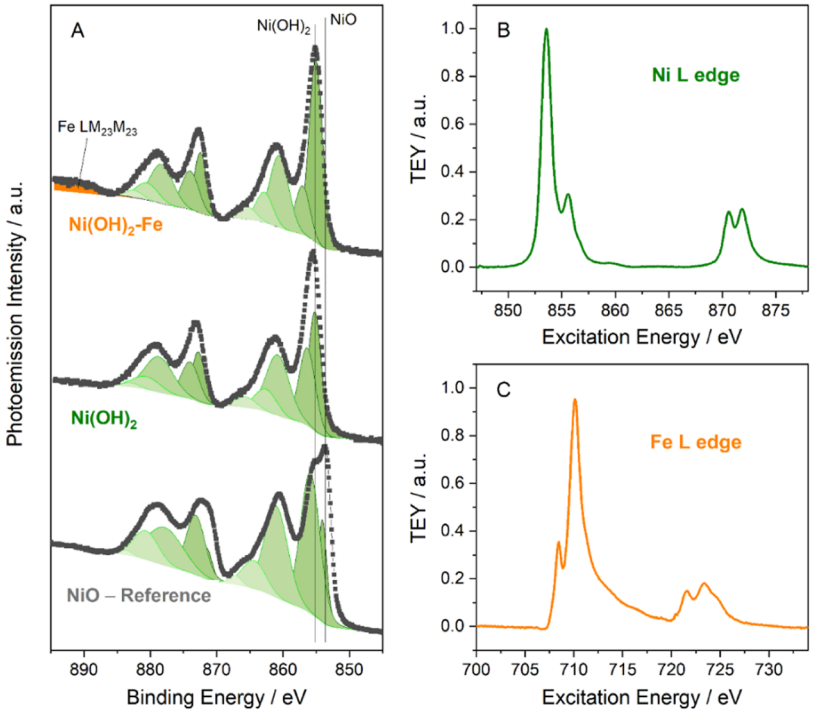

Figure 3. Ni 2p photoemission spectra of pristine $Ni(OH)_2$-Fe, $Ni(OH)_2$, and NiO reference powders obtained under UHV condition (A); Ni L edge (B) and Fe L edge (C) of $Ni(OH)_2$-Fe under low-vacuum condition acquired from X-ray absorption measurements. Linear background was subtracted, and intensities are normalized to the maximum intensity.

should note that 486 hrs electrolysis operation was carried out at constant current density, which is less stressful than dynamic operation conditions.[38] Therefore, the performance stability of AEM electrolyzers in various scenarios is to be further

https://doi.org/10.1021/acsaem.1c03761
ACS Appl. Energy Mater. XXXX, XXX, XXX−XXX

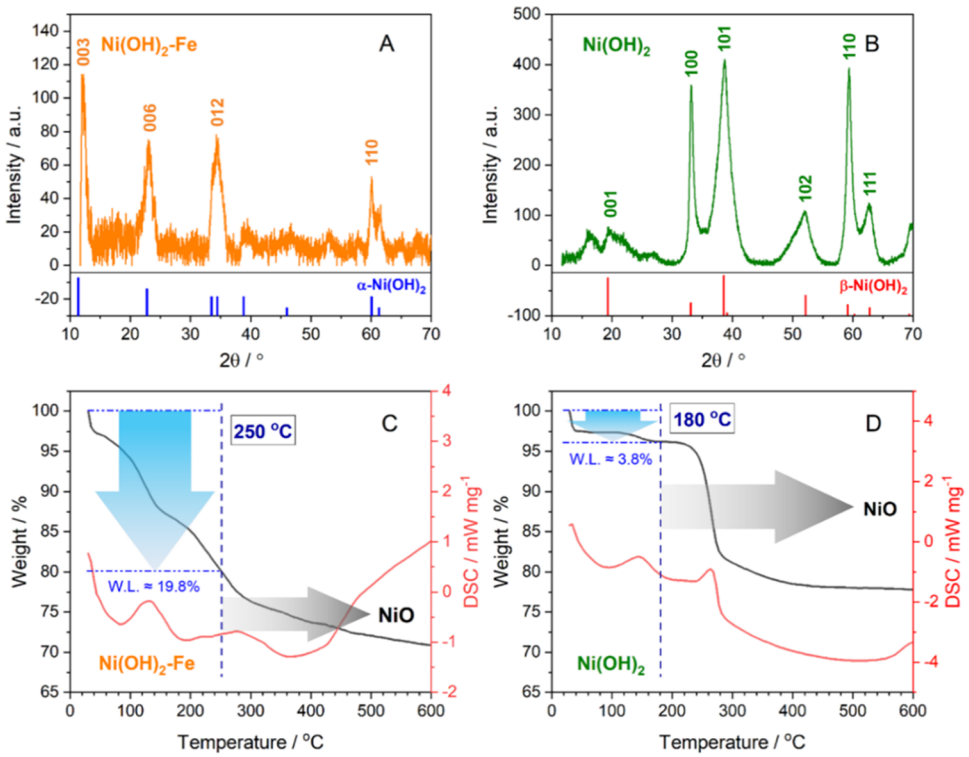

Figure 4. X-ray diffraction pattern of the $Ni(OH)_2$-Fe (A) and $Ni(OH)_2$ (B) powder (blue lines and red lines correspond to the ICDD no. 00-038-0715 card of α-$Ni(OH)_2$ and ICDD no. 00-057-0907 card of β-$Ni(OH)_2$); thermogravimetric analysis of $Ni(OH)_2$-Fe (C) and $Ni(OH)_2$ (D).

investigated. In addition, carbon nanotubes were used in these electrolysis cell measurements at both cathode and anode to attain the electron conductivity of the catalytic layers needed to demonstrate the target performance. For industrially relevant operation times of >50 000 h, carbon components may not be stable enough, requiring either carbon-free anodes or demonstration of stability on such time scales.

Further efforts were devoted to understand the anode $Ni(OH)_2$-Fe catalyst and specifically the role of the Fe dopant. For this purpose, $Ni(OH)_2$ is synthesized with the same approach, and care is taken to avoid Fe contamination during the preparation. Figure 2A shows the fingerprint cyclic voltammograms (CV) of both $Ni(OH)_2$-Fe and $Ni(OH)_2$ in 0.1 M NaOH electrolyte, with the clearly observable $Ni(OH)_2$/NiOOH redox transition (see the inset of Figure 2A) for the $Ni(OH)_2$ sample. In agreement with previous publications,[10,12,18,39] Fe doping leads to a positive shift of the $Ni^{2+}/Ni^{3+(4+)}$ redox peaks and a significantly higher OER activity. Previous publications tentatively attributed these changes to the charge transfer from Ni to Fe cations[39] and to the influence of Fe on the trigonal distortion of the octahedral symmetry at the Ni centers.[40] Since metal redox switching is an essential step of the OER catalytic cycle,[18,41−44] we studied the scan rate dependence of the $Ni(OH)_2$/NiOOH transition, for both samples, in a three-electrode cell with a liquid electrolyte to gain insight into the influence of Fe doping on its kinetics. Results are shown in Figure 2B,C for $Ni(OH)_2$-Fe and $Ni(OH)_2$, respectively. As the anodic peak for the Fe-doped sample overlaps with the OER current, in Figure 2D, we compare the effect of the scan rate on the cathodic peak potential for both samples. One may notice a significantly smaller negative shift of the peak potential with the scan rate for the Fe-doped sample, evidencing faster kinetics of the redox transition, the latter underpinning its higher OER activity. In addition, Figure 2E shows the influence of the sweep rate (υ) on the anodic (only for $Ni(OH)_2$) and cathodic (for both samples) peak currents. The observed $i_p \sim \sqrt{\upsilon}$ dependence is in line with the previous publications and confirms that the $Ni^{2+}/Ni^{3+(4+)}$ redox transition is coupled with the ion (H^+[45,46] or OH^-[46]) transport in the $Ni(OH)_2$ lattice. Furthermore, the cathodic peak current is smaller for the Fe-doped sample and shows a different slope confirming that the generated $Ni^{3+/4+}$ species are consumed in the following step(s) resulting in the oxygen evolution.[47−50] Consequently, the cathodic charge is also smaller for the Fe-doped sample (Figure 2F) and the difference between the doped and undoped samples is accentuated by the increase of scan rate (Figure S5, see the SI), the latter confirming faster kinetics of this subsequent step for the Fe-doped sample.

The pristine materials were analyzed using X-ray photoelectron spectroscopy (XPS) under ultrahigh-vacuum (UHV) conditions, to determine their surface composition and the oxidation state of the elements. Figure 3A shows the Ni2p spectra of $Ni(OH)_2$-Fe and $Ni(OH)_2$, and—for comparison—a NiO reference. The spectra have been fitted with five components each, to deconvolute the main signal(s) between 850 and 862 eV, as the lower resolution of the measurements prevents detailed distinguishing between the individual signals of the frequently discussed multiplet structure of the Ni2p photoemission signal. The interpretation of the main signals follows the fundamental works of Grosvenor et al.[51,52] The XP spectra of both the Fe-doped and undoped samples correspond well to those reported for $Ni(OH)_2$, confirming the Ni^{2+} oxidation state,[51,52] albeit the expected asymmetric envelope for $Ni(OH)_2$ could not be resolved. An additional Fe Auger peak was observed in the $Ni(OH)_2$-Fe sample at ~889 eV, while absent in the $Ni(OH)_2$ counterpart, in agreement with the spectral features of Fe2p electrons and Fe^{3+} oxidation state

https://doi.org/10.1021/acsaem.1c03761
ACS Appl. Energy Mater. XXXX, XXX, XXX−XXX

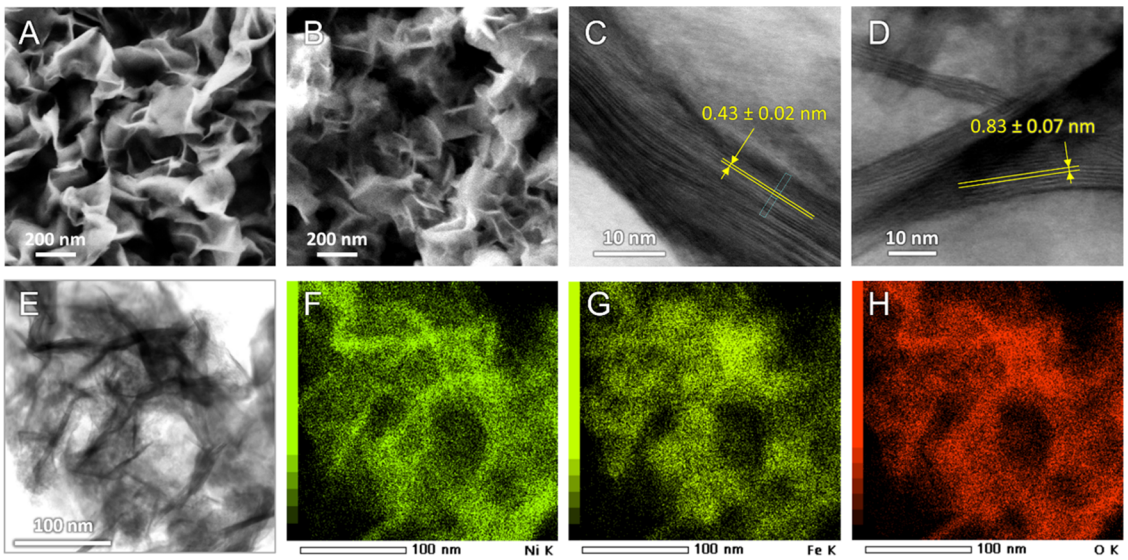

Figure 5. SEM images of $Ni(OH)_2$ (A) and $Ni(OH)_2$-Fe (B); bright-field HR-TEM images of $Ni(OH)_2$ (C) and $Ni(OH)_2$-Fe (D); BF-STEM image of $Ni(OH)_2$-Fe (E) and its corresponding element mappings of Ni (F), Fe (G), and O (H).

(see Figure S9, SI). The $Ni(OH)_2$-Fe sample was further analyzed by the near-edge X-ray absorption fine structure (NEXAFS) spectroscopy under low-vacuum condition (*ca.* 10^{-2} mbar). According to the spectral shape and peak position, the Ni L edge shown in Figure 3B corresponds to Ni^{2+} while the Fe L edge in Figure 3C to Fe^{3+}, in line with the XPS results.

The crystalline structure of the pristine samples was determined with X-ray powder diffraction (XRD), the diffraction patterns are shown in Figure 4A,B. It is interesting to note that the Fe-doped and undoped samples crystallize in different phases: α-$Ni(OH)_2$ phase for the Fe-doped and β-$Ni(OH)_2$ phase for the undoped sample. Fe in the doped sample does not appear as a separate phase, confirming that, in agreement with the literature, Fe occupies Ni^{2+} lattice positions in the α-$Ni(OH)_2$ structure.[18,19,53] This conclusion is also confirmed by the elemental mapping shown in Figure 5 and discussed below. While according to the Bode scheme of $Ni(OH)_2$/NiOOH the α-$Ni(OH)_2$ phase is the initial structure of Ni hydroxide,[54] the β-$Ni(OH)_2$ phase may be ascribed to the aging effect due to the electrochemical dissolution−precipitation method used to prepare the catalyst that takes 80 hrs for each sample.[45,55] Even though attention was paid to avoid Fe contamination in the $Ni(OH)_2$ sample and neither XRD nor UHV-XPS provided evidence for the presence of Fe traces, a tiny amount of Fe was still found by inductively coupled plasma optical emission spectrometry (ICP-OES, see the SI) and scanning transmission electron microscopy (STEM, Figure S10, see the SI). STEM/EDX results indicate that contrary to the Fe-doped sample, the unintentionally present Fe (which, according to the literature data, is hard to avoid[12,55]) appears as a separated minority phase in the undoped sample (Figure S10, see the SI).

Obtaining α-$Ni(OH)_2$ is possible through three approaches according to previous studies: (1) overcharge of β-$Ni(OH)_2$ phase;[54] (2) incorporation of anions into β-$Ni(OH)_2$, e.g., SO_4^{2-};[56] (3) partial substitution of Ni in β-$Ni(OH)_2$ by secondary metal, e.g., Co, Cd, or Fe.[53,57,58] The first two methods have been reported to yield a structure-instable α-$Ni(OH)_2$ phase in an alkaline medium that quickly aged into β-$Ni(OH)_2$[54,56] while secondary metal-doped α-$Ni(OH)_2$ is structure-stable.[57,58] Thermogravimetric analyses (TGA) in Ar atmosphere were carried out on both $Ni(OH)_2$-Fe and $Ni(OH)_2$; the results are shown in Figure 4C,D, respectively. $Ni(OH)_2$-Fe shows the typical α-$Ni(OH)_2$ phase TGA behavior;[56] the adsorbed and a part of intercalated water molecules in the interlayer spacing are removed below 160 °C, followed by the second stage of intercalated H_2O release in the temperature interval from 160 to *ca.* 250 °C. At higher temperatures, the phase transformation to NiO starts. An overall water loss of 19.8% is recorded for $Ni(OH)_2$-Fe. The TGA behavior of $Ni(OH)_2$ electrochemically synthesized in this work is similar to the chemically synthesized catalyst by Mani et al,[59] both possessing the β-$Ni(OH)_2$ structure. According to TGA, all water molecules were removed in one single step and transformation to NiO starts at 180 °C.[59] For $Ni(OH)_2$, only 3.8% water loss was recorded. The significant difference of the water content in the Fe-doped and undoped samples implies the higher amount of H_2O intercalation between α-$Ni(OH)_2$ slabs of $Ni(OH)_2$-Fe, suggesting a possibility that intercalated H_2O molecule is another facilitator that is relating to the kinetics of the redox transition and the following chemical step leading to the excellent oxygen evolution activity as discussed above. Further in situ measurements and theoretical computation work are needed to validate this hypothesis.

The morphologies of $Ni(OH)_2$ and $Ni(OH)_2$-Fe powders analyzed by scanning electron microscopy (SEM) are displayed in Figure 5A,B. Both samples show the flake-like structure—a typical feature of electrochemically prepared Ni(Fe) hydroxides.[12,39,60] $Ni(OH)_2$ contains larger flakes, while $Ni(OH)_2$-Fe contains more shattered flakes with a smaller size. The interplanar spacing in the layered structure is determined from high-resolution transmission electron microscopy (HR-TEM) images shown in Figure 5C,D, as 0.43 ± 0.02 nm for $Ni(OH)_2$ and 0.83 ± 0.07 nm for $Ni(OH)_2$-Fe (see intensity profiles in Figures S11 and S12 in the SI), which is in good agreement with the (001) interplanar spacing of β-$Ni(OH)_2$ and α-$Ni(OH)_2$,[61] respectively. These values are in line with XRD analyses. The irregular layers indicate the

https://doi.org/10.1021/acsaem.1c03761
ACS Appl. Energy Mater. XXXX, XXX, XXX−XXX

turbostratic structure in both samples; for α-$Ni(OH)_2$, it was caused by the presence of intercalated water molecules in between the $Ni(OH)_2$ slabs, where H_2O does not occupy fixed lattice points. β-$Ni(OH)_2$, being the product of the α-$Ni(OH)_2$ phase aging, also forms a turbostratic structure. The results of HR-TEM indicate that the outermost surface in both $Ni(OH)_2$ and $Ni(OH)_2$-Fe sample is dominated by the (001) plane, suggesting the latter to serve as the active surface for the OER catalysis. Figure 5E shows the bright-field STEM image of $Ni(OH)_2$-Fe and its corresponding element mapping of Ni, Fe, and O are given in Figure 5F−H. Well-distributed Ni, Fe, and O traces indicate that Fe is homogeneously incorporated into the crystalline structure of $Ni(OH)_2$-Fe, which is essential to ensure its superior OER activity[60] and, in our opinion, it is also a key factor for maintaining the structure-stable α-$Ni(OH)_2$ phase.

To identify the active site for the OER on the (001) plane and rationalize the effect of Fe inclusion on the OER mechanism and pathway, spin-polarized DFT + U computations were carried out for pure γ-NiOOH and γ-NiOOH-Fe (see the SI for model systems and computational details). Even though $Ni^{3+/4+}$ were not observed by our *in situ* XAS measurements (Figure S6, see the SI), which was explained by its small quantity during the spectroscopic recording time and the fast consumption by the following catalytic process, these species are believed to play a significant role and were confirmed by Görlin et al.[18] Therefore, DFT was carried out in different scenarios containing Ni^{3+}, Ni^{4+}, and Fe^{3+}. Energy diagrams for the OER on these surfaces were generated with the computational hydrogen electrode (CHE) scheme.[62] In this scheme, the electrochemical potential of OH^- in solution, μ_{OH^-}, at a given electrode potential can be derived as (see details in the SI),

$$\mu_{OH^-} - \mu_e = \mu^0_{H_2O} - \frac{1}{2}\mu^0_{H_2} + eU_{RHE} \quad (1)$$

where μ_e is the electrochemical potential of the electrons, $\mu^0_{H_2} = E_{H_2}$ is the DFT-calculated energy of molecular hydrogen in the gas phase, $\mu^0_{H_2O}$ is that for a single water molecule in the liquid phase, and U_{RHE} is the electrode potential on the reversible hydrogen electrode (RHE) scale.

We considered a widely accepted reaction pathway for the OER, which under alkaline conditions proceeds *via* four OH^--coupled electron transfer steps (although some publications evidence contribution of a proton-decoupled electron transfer step to the OER on NiOOH[63]):

$$OH^- + * \rightarrow OH^* + e^- \quad \text{(step 1)}$$

$$OH^* + OH^- \rightarrow O^* + H_2O + e^- \quad \text{(step 2)}$$

$$O^* + OH^- \rightarrow OOH^* + e^- \quad \text{(step 3)}$$

$$OOH^* + OH^- \rightarrow * + O_2 + H_2O + e^- \quad \text{(step 4)}$$

and involves three intermediates, OH*, O*, and OOH*. The OER mechanism had been studied on the high-index facet of γ-NiOOH-Fe$(01\bar{1}2)$,[19] and recently on the (001) facet of pure β-NiOOH.[64] On the (001) facet, the OER involves surface deprotonation (step 2)—a pH-dependent process that has also been observed experimentally[63]—and oxygen vacancy formation (step 4), which follows upon desorption of molecular oxygen from an active site. This mechanism is demonstrated in Figure 6A. Next, the OER free energy diagram, as shown in Figure 6B, was constructed by calculating the reaction energy

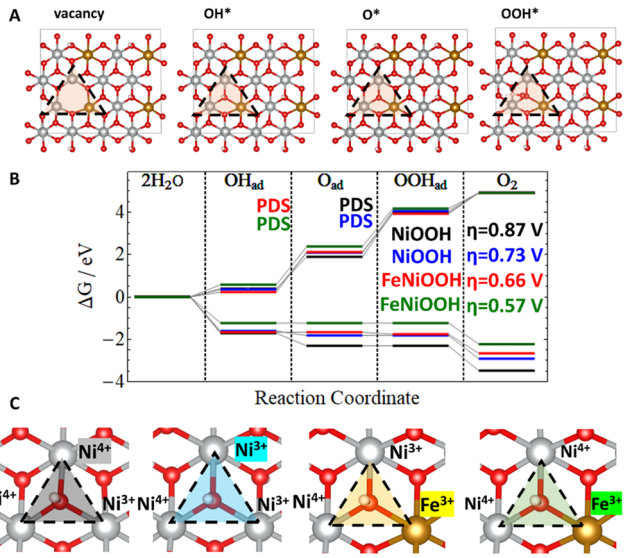

Figure 6. (A) Top view of the optimized structures for the OER mechanism on γ-$Fe_{0.25}Ni_{0.75}OOH$ (001). Gray, brown, red, and white atoms represent Ni, Fe, O, and H, respectively. (B) Free energy diagram of the OER on γ-NiOOH(001) with local arrangement of Ni^{3+} with two Ni^{4+} (black), two Ni^{3+} with one Ni^{4+} (blue), and γ-$Fe_{0.25}Ni_{0.75}OOH$(001) with local vicinity of Fe^{3+} with Ni^{3+} and Ni^{4+} (red), and that for local arrangement of Fe^{3+} with two Ni^{4+} (green). (C) Representation of the active site of these systems and the projected oxidation state for the case of OH*.

of each elementary step, ΔG, (see Table S2 for the values). The thermodynamic overpotential, η, was calculated using[62]

$$\eta = \frac{\max(\Delta G_1, \Delta G_2, \Delta G_3, \Delta G_4)}{e} - 1.23\ (V) \quad (2)$$

For the pure γ-NiOOH(001), an overpotential of 0.73 V was obtained, which corresponds to the potential-determining step (PDS) of OOH* formation. This relates to an active site with two Ni^{3+} and one Ni^{4+} (see Figure 6C). This value is in agreement with the reported overpotential of 0.75 V by Tkalych et al.[65] and 0.69 V by Govind Rajan et al.[64] on β-NiOOH(001) using the PBE + U (U = 5.5 eV) method. For this surface, we also examined an active site with two Ni^{4+} and one Ni^{3+} by removing an extra hydrogen atom from the bottom of the surface (see Figure S2). On this site, the thermodynamic overpotential was increased to 0.87 V.

Likewise, for the γ-NiOOH-Fe(001), two different surface configurations were considered, as shown in Figure 6C. In the first system, Fe^{3+} forms the active site configuration in the vicinity with one Ni^{3+} and one Ni^{4+}. In the second system, an extra hydrogen atom was removed from the bottom of the surface to form two Ni^{4+} in neighboring with Fe^{3+} (also, see Figure S2). The oxidation states were confirmed by calculating the atom-projected magnetic moment as well as the d-projected density of states (see Table S1 and Figure S3). Next, the reaction energies were computed for these two surfaces and the OER energy diagram was constructed. Figure 6B compares the pathways for these two systems. Although, in both cases, charge transfer occurs from Fe^{3+} to the OER intermediates (see Table S3 for the projected magnetic moments), the local arrangement of Fe^{3+} with two Ni^{4+} leads

https://doi.org/10.1021/acsaem.1c03761
ACS Appl. Energy Mater. XXXX, XXX, XXX−XXX

to the lower overpotential of 0.57 V compared to 0.66 V for Fe^{3+} in the neighboring of Ni^{3+} and Ni^{4+}. This suggests that the formation of Ni^{4+} for the γ-NiOOH phase and its combination with Fe^{3+} plays an important role in the activity of the (001) facet of γ-NiOOH-Fe.

4. CONCLUSIONS

In summary, a high-performance AEM electrolyzer equipped with $Ni(OH)_2$-Fe anode is reported. The main aim was to further our understanding of the excellent OER activity of Fe-doped Ni hydroxide and the role of Fe. We found that the (001) crystal plane is the dominating catalysis surface for the OER in both $Ni(OH)_2$-Fe and $Ni(OH)_2$ samples, composed of the α-$Ni(OH)_2$ and β-$Ni(OH)_2$ phases, respectively. Fe-doping stabilizes the α-$Ni(OH)_2$ phase, which is otherwise structure-unstable and converts to the β-$Ni(OH)_2$ phase upon aging. The kinetics of the $Ni(OH)_2$/NiOOH redox transition was found to be faster for the Fe-doped α-$Ni(OH)_2$ phase compared to the β-$Ni(OH)_2$ phase, which may be attributed to the presence of water in the interlayer spacing and to the ensuing structure flexibility of the α-phase. The subsequent step of the $Ni^{3+/4+}$ reaction with the electrolyte (OH^-) is also faster for the Fe-doped sample compared to the undoped one, as evidenced by the scan rate dependence. Moreover, DFT + U computations were carried out on the NiOOH-Fe(001) plane, revealing that the local arrangement of Fe^{3+} with two Ni^{4+} on an oxo vacant site on the (001) plane increases the OER activity. These findings could serve as a guidance for further advancing the anode catalyst of AEM electrolyzers.

■ ASSOCIATED CONTENT

Supporting Information

The Supporting Information is available free of charge at https://pubs.acs.org/doi/10.1021/acsaem.1c03761.

Additional physical characterization (UHV-XPS, STEM, ICP-OES) and RDE measurement, operando X-ray absorption spectroscopy (XAS), the details of DFT + U computations (PDF)

■ AUTHOR INFORMATION

Corresponding Author

Li Wang − *Institute of Engineering Thermodynamics, German Aerospace Center (DLR), 70569 Stuttgart, Germany;* orcid.org/0000-0002-4129-7125; Email: li.wang@dlr.de

Authors

Viktoriia A. Saveleva − *Institut de Chimie et Procédés pour l'Energie, l'Environnement et la Santé, UMR 7515 du CNRS-Université de Strasbourg, 67087 Strasbourg, France;* Present Address: ESRF—The European Synchrotron, 71 Avenue des Martyrs, 38043 Grenoble, France

Mohammad J. Eslamibidgoli − *Theory and Computation of Energy Materials (IEK-13), Institute of Energy and Climate Research, Forschungszentrum Jülich GmbH, 52425 Jülich, Germany*

Denis Antipin − *Institut de Chimie et Procédés pour l'Energie, l'Environnement et la Santé, UMR 7515 du CNRS-Université de Strasbourg, 67087 Strasbourg, France;* Present Address: Nachwuchsgruppe Gestaltung des Sauerstoffentwicklungsmechanismus, Helmholtz-Zentrum Berlin für Materialien und Energie GmbH, Hahn-Meitner-Platz 1, 14109 Berlin, Germany

Corinne Bouillet − *Institut de Physique et Chimie des Matériaux de Strasbourg (IPCMS), UMR 7504 CNRS, Université de Strasbourg, 67034 Strasbourg, France*

Indro Biswas − *Institute of Engineering Thermodynamics, German Aerospace Center (DLR), 70569 Stuttgart, Germany*

Aldo S. Gago − *Institute of Engineering Thermodynamics, German Aerospace Center (DLR), 70569 Stuttgart, Germany;* orcid.org/0000-0001-7000-171X

Seyed S. Hosseiny − *Institute of Engineering Thermodynamics, German Aerospace Center (DLR), 70569 Stuttgart, Germany*

Pawel Gazdzicki − *Institute of Engineering Thermodynamics, German Aerospace Center (DLR), 70569 Stuttgart, Germany*

Michael H. Eikerling − *Theory and Computation of Energy Materials (IEK-13), Institute of Energy and Climate Research, Forschungszentrum Jülich GmbH, 52425 Jülich, Germany; Chair of Theory and Computation of Energy Materials, Faculty of Georesources and Materials Engineering, RWTH Aachen University, 52062 Aachen, Germany;* orcid.org/0000-0002-0764-8948

Elena R. Savinova − *Institut de Chimie et Procédés pour l'Energie, l'Environnement et la Santé, UMR 7515 du CNRS-Université de Strasbourg, 67087 Strasbourg, France;* orcid.org/0000-0001-7304-6825

K. Andreas Friedrich − *Institute of Engineering Thermodynamics, German Aerospace Center (DLR), 70569 Stuttgart, Germany; Institute of Building Energetics, Thermal Engineering and Energy Storage (IGTE), University of Stuttgart, 70569 Stuttgart, Germany;* orcid.org/0000-0002-2968-5029

Complete contact information is available at: https://pubs.acs.org/10.1021/acsaem.1c03761

Author Contributions

L.W., V.S., E.R.S., and K.A.F. conceived and initiated the project. L.W. synthesized the material. D.A. carried out the liquid cell electrochemical measurements. L.W. manufactured the electrodes and performed the electrolyzer test. I.B. and P.G. conducted the UHV-XPS analysis. V.S. and E.R.S. performed the *ex situ*/operando NAP-XPS and XAS measurements. C.U. and E.R.S. carried out the TEM/STEM analysis. M.J.E. and M.E. performed the DFT simulation. S.S.H. involved in the discussion of catalyst preparation. A.S.G. involved in several discussions. L.W. drafted the manuscript with contributions from all co-authors. The final version was reviewed and proofed by all of the authors for publication.

Notes

The authors declare no competing financial interest.

■ ACKNOWLEDGMENTS

The research leading to these results has received funding from the European Union's Seventh Framework Programme (FP7/2007-2013) for Fuel Cell and Hydrogen Joint Technology Initiative under Grant No. 621237 (INSIDE) and funding from the European Union's Horizon 2020 research and innovation programme under grant agreement no. 761093 (LOTER.CO2M). The authors gratefully acknowledge the Gauss Centre for Supercomputing e.V. (www.gauss-centre.eu) for funding this project by providing computing time through the John von Neumann Institute for Computing (NIC) on the

GCS Supercomputer JUWELS[66] at Jülich Supercomputing Centre (JSC). They thank Ian Stark (Scott Precision Wire Ltd, U.K.) for providing NiFe wire; Ina Plock for her support on SEM and EDS analyses; Oliver Freitag for the XRD measurements and TGA analyses; and Heike Fingerle (University of Stuttgart) for the ICP-OES analyses. L.W. thanks Dr. Rémi Costa for the fruitful discussion and for providing electrolyzer component materials for testing. L.W. appreciates Dr. Julio C. Garcia-Navarro for providing test bench to conduct the electrolyzer tests. I.B. is grateful to Dr. Mathias Schulze for valuable discussions on the properties of the nickel surface. The authors thank the BESSYII/HZB (Berlin, Germany) for allocating the beamline time for the X-ray absorption measurements as well as Dr. Detre Teschner, Dr. Jean-Jacques Gallet, and Dr. Fabrice Bournel for assisting during these measurements. Sanchit Gupta is acknowledged for the language proof.

REFERENCES

(1) Carmo, M.; Fritz, D. L.; Mergel, J.; Stolten, D. A comprehensive review on PEM water electrolysis. *Int. J. Hydrogen Energy* **2013**, *38*, 4901−4934.
(2) Paoli, E. A.; Masini, F.; Frydendal, R.; Deiana, D.; Schlaup, C.; Malizia, M.; Hansen, T. W.; Horch, S.; Stephens, I. E. L.; Chorkendorff, I. Oxygen evolution on well-characterized mass-selected Ru and RuO_2 nanoparticles. *Chem. Sci.* **2015**, *6*, 190−196.
(3) Wang, L.; Weissbach, T.; Reissner, R.; Ansar, A.; Gago, A. S.; Holdcroft, S.; Friedrich, K. A. High Performance Anion Exchange Membrane Electrolysis Using Plasma-Sprayed, Non-Precious-Metal Electrodes. *ACS Appl. Energy Mater.* **2019**, *2*, 7903−7912.
(4) Vincent, I.; Bessarabov, D. Low cost hydrogen production by anion exchange membrane electrolysis: A review. *Renewable Sustainable Energy Rev.* **2018**, *81*, 1690−1704.
(5) Vincent, I.; Kruger, A.; Bessarabov, D. Development of efficient membrane electrode assembly for low cost hydrogen production by anion exchange membrane electrolysis. *Int. J. Hydrogen Energy* **2017**, *42*, 10752−10761.
(6) Chen, P.; Hu, X. High-Efficiency Anion Exchange Membrane Water Electrolysis Employing Non-Noble Metal Catalysts. *Adv. Energy Mater.* **2020**, *10*, No. 2002285.
(7) Fabbri, E.; Nachtegaal, M.; Binninger, T.; Cheng, X.; Kim, B. J.; Durst, J.; Bozza, F.; Graule, T.; Schaublin, R.; Wiles, L.; Pertoso, M.; Danilovic, N.; Ayers, K. E.; Schmidt, T. J. Dynamic surface self-reconstruction is the key of highly active perovskite nano-electrocatalysts for water splitting. *Nat. Mater.* **2017**, *16*, 925−931.
(8) Li, D.; Park, E. J.; Zhu, W.; Shi, Q.; Zhou, Y.; Tian, H.; Lin, Y.; Serov, A.; Zulevi, B.; Baca, E. D.; Fujimoto, C.; Chung, H. T.; Kim, Y. S. Highly quaternized polystyrene ionomers for high performance anion exchange membrane water electrolysers. *Nat. Energy* **2020**, *5*, 378−385.
(9) Ayers, K.; Danilovic, N.; Ouimet, R.; Carmo, M.; Pivovar, B.; Bornstein, M. Perspectives on Low-Temperature Electrolysis and Potential for Renewable Hydrogen at Scale. *Annu. Rev. Chem. Biomol. Eng.* **2019**, *10*, 219−239.
(10) Dionigi, F.; Strasser, P. NiFe-Based (Oxy)hydroxide Catalysts for Oxygen Evolution Reaction in Non-Acidic Electrolytes. *Adv. Energy Mater.* **2016**, *6*, No. 1600621.
(11) Corrigan, D. A. The Catalysis of the Oxygen Evolution Reaction by Iron Impurities in Thin Film Nickel Oxide Electrodes. *J. Electrochem. Soc.* **1987**, *134*, 377−384.
(12) Trotochaud, L.; Young, S. L.; Ranney, J. K.; Boettcher, S. W. Nickel-iron oxyhydroxide oxygen-evolution electrocatalysts: the role of intentional and incidental iron incorporation. *J. Am. Chem. Soc.* **2014**, *136*, 6744−53.
(13) Schoen, M. A. W.; Calderon, O.; Randell, N. M.; Jimenez-Villegas, S.; Daly, K. M.; Chernikov, R.; Trudel, S. Local structural changes in polyamorphous (Ni,Fe)O_x electrocatalysts suggest a dual-site oxygen evolution mechanism. *J. Mater. Chem. A* **2021**, *9*, 13252−13262.
(14) Bai, L.; Lee, S.; Hu, X. Spectroscopic and Electrokinetic Evidence for a Bifunctional Mechanism of the Oxygen Evolution Reaction. *Angew. Chem., Int. Ed.* **2021**, *60*, 3095−3103.
(15) Zhang, N.; Feng, X.; Rao, D.; Deng, X.; Cai, L.; Qiu, B.; Long, R.; Xiong, Y.; Lu, Y.; Chai, Y. Lattice oxygen activation enabled by high-valence metal sites for enhanced water oxidation. *Nat. Commun.* **2020**, *11*, No. 4066.
(16) Lee, S.; Banjac, K.; Lingenfelder, M.; Hu, X. Oxygen Isotope Labeling Experiments Reveal Different Reaction Sites for the Oxygen Evolution Reaction on Nickel and Nickel Iron Oxides. *Angew. Chem., Int. Ed.* **2019**, *58*, 10295−10299.
(17) Li, N.; Bediako, D. K.; Hadt, R. G.; Hayes, D.; Kempa, T. J.; von Cube, F.; Bell, D. C.; Chen, L. X.; Nocera, D. G. Influence of iron doping on tetravalent nickel content in catalytic oxygen evolving films. *Proc. Natl. Acad. Sci. U.S.A.* **2017**, *114*, 1486−1491.
(18) Görlin, M.; Chernev, P.; Ferreira de Araujo, J.; Reier, T.; Dresp, S.; Paul, B.; Krahnert, R.; Dau, H.; Strasser, P. Oxygen Evolution Reaction Dynamics, Faradaic Charge Efficiency, and the Active Metal Redox States of Ni-Fe Oxide Water Splitting Electrocatalysts. *J. Am. Chem. Soc.* **2016**, *138*, 5603−14.
(19) Friebel, D.; Louie, M. W.; Bajdich, M.; Sanwald, K. E.; Cai, Y.; Wise, A. M.; Cheng, M. J.; Sokaras, D.; Weng, T. C.; Alonso-Mori, R.; Davis, R. C.; Bargar, J. R.; Norskov, J. K.; Nilsson, A.; Bell, A. T. Identification of highly active Fe sites in (Ni,Fe)OOH for electrocatalytic water splitting. *J. Am. Chem. Soc.* **2015**, *137*, 1305−13.
(20) Burke, M. S.; Enman, L. J.; Batchellor, A. S.; Zou, S.; Boettcher, S. W. Oxygen Evolution Reaction Electrocatalysis on Transition Metal Oxides and (Oxy)hydroxides: Activity Trends and Design Principles. *Chem. Mater.* **2015**, *27*, 7549−7558.
(21) Jung, S. C.; Sim, S. L.; Soon, Y. W.; Lim, C. M.; Hing, P.; Jennings, J. R. Synthesis of nanostructured β-Ni$(OH)_2$ by electrochemical dissolution-precipitation and its application as a water oxidation catalyst. *Nanotechnology* **2016**, *27*, No. 275401.
(22) Hesse, R.; Chasse, T.; Szargan, R. Peak shape analysis of core level photoelectron spectra using UNIFIT for WINDOWS. *Fresenius' J. Anal. Chem.* **1999**, *365*, 48−54.
(23) Yeh, J. J.; Lindau, I. Atomic subshell photoionization cross sections and asymmetry parameters: $1 \leq Z \leq 103$. *At. Data Nucl. Data Tables* **1985**, *32*, 1−155.
(24) Suntivich, J.; Gasteiger, H. A.; Yabuuchi, N.; Yang, S.-H. Electrocatalytic Measurement Methodology of Oxide Catalysts Using a Thin-Film Rotating Disk Electrode. *J. Electrochem. Soc.* **2010**, *157*, B1263−B1268.
(25) Pavel, C. C.; Cecconi, F.; Emiliani, C.; Santiccioli, S.; Scaffidi, A.; Catanorchi, S.; Comotti, M. Highly efficient platinum group metal free based membrane-electrode assembly for anion exchange membrane water electrolysis. *Angew. Chem., Int. Ed.* **2014**, *53*, 1378−1381.
(26) Kresse, G.; Furthmüller, J. Efficiency of ab-initio total energy calculations for metals and semiconductors using a plane-wave basis set. *Comput. Mater. Sci.* **1996**, *6*, 15−50.
(27) Kresse, G.; Furthmüller, J. Efficient iterative schemes for ab initio total-energy calculations using a plane-wave basis set. *Phys. Rev. B* **1996**, *54*, 11169−11185.
(28) Blöchl, P. E. Projector augmented-wave method. *Phys. Rev. B* **1994**, *50*, 17953−17979.
(29) Perdew, J. P.; Burke, K.; Ernzerhof, M. Generalized Gradient Approximation Made Simple. *Phys. Rev. Lett.* **1996**, *77*, 3865−3868.
(30) Dudarev, S. L.; Botton, G. A.; Savrasov, S. Y.; Humphreys, C. J.; Sutton, A. P. Electron-energy-loss spectra and the structural stability of nickel oxide: An LSDA+U study. *Phys. Rev. B* **1998**, *57*, 1505−1509.
(31) Cococcioni, M.; de Gironcoli, S. Linear response approach to the calculation of the effective interaction parameters in the LDA+U method. *Phys. Rev. B* **2005**, *71*, No. 035105.

https://doi.org/10.1021/acsaem.1c03761
ACS Appl. Energy Mater. XXXX, XXX, XXX−XXX

(32) Li, Y.-F.; Selloni, A. Mechanism and Activity of Water Oxidation on Selected Surfaces of Pure and Fe-Doped NiO_x. *ACS Catal.* **2014**, *4*, 1148−1153.
(33) Monkhorst, H. J.; Pack, J. D. Special points for Brillouin-zone integrations. *Phys. Rev. B* **1976**, *13*, 5188−5192.
(34) Hackemüller, F. J.; Borgardt, E.; Panchenko, O.; Müller, M.; Bram, M. Manufacturing of Large-Scale Titanium-Based Porous Transport Layers for Polymer Electrolyte Membrane Electrolysis by Tape Casting. *Adv. Eng. Mater.* **2019**, *21*, No. 1801201.
(35) Kaczur, J. J.; Yang, H.; Liu, Z.; Sajjad, S. D.; Masel, R. I. Carbon Dioxide and Water Electrolysis Using New Alkaline Stable Anion Membranes. *Front. Chem.* **2018**, *6*, No. 263.
(36) Koshikawa, H.; Murase, H.; Hayashi, T.; Nakajima, K.; Mashiko, H.; Shiraishi, S.; Tsuji, Y. Single Nanometer-Sized NiFe-Layered Double Hydroxides as Anode Catalyst in Anion Exchange Membrane Water Electrolysis Cell with Energy Conversion Efficiency of 74.7% at 1.0 A cm^{-2}. *ACS Catal.* **2020**, *10*, 1886−1893.
(37) McKone, J. R.; Sadtler, B. F.; Werlang, C. A.; Lewis, N. S.; Gray, H. B. Ni−Mo Nanopowders for Efficient Electrochemical Hydrogen Evolution. *ACS Catal.* **2013**, *3*, 166−169.
(38) Papakonstantinou, G.; Algara-Siller, G.; Teschner, D.; Vidaković-Koch, T.; Schlögl, R.; Sundmacher, K. Degradation study of a proton exchange membrane water electrolyzer under dynamic operation conditions. *Appl. Energy* **2020**, *280*, No. 115911.
(39) Enman, L. J.; Burke, M. S.; Batchellor, A. S.; Boettcher, S. W. Effects of Intentionally Incorporated Metal Cations on the Oxygen Evolution Electrocatalytic Activity of Nickel (Oxy)hydroxide in Alkaline Media. *ACS Catal.* **2016**, *6*, 2416−2423.
(40) Smith, R. D. L.; Pasquini, C.; Loos, S.; Chernev, P.; Klingan, K.; Kubella, P.; Mohammadi, M. R.; González-Flores, D.; Dau, H. Geometric distortions in nickel (oxy)hydroxide electrocatalysts by redox inactive iron ions. *Energy Environ. Sci.* **2018**, *11*, 2476−2485.
(41) Kuznetsov, D. A.; Han, B.; Yu, Y.; Rao, R. R.; Hwang, J.; Román-Leshkov, Y.; Shao-Horn, Y. Tuning Redox Transitions via Inductive Effect in Metal Oxides and Complexes, and Implications in Oxygen Electrocatalysis. *Joule* **2018**, *2*, 225−244.
(42) Lyons, M. E. G.; Doyle, R. L.; Godwin, I.; O'Brien, M.; Russell, L. Hydrous Nickel Oxide: Redox Switching and the Oxygen Evolution Reaction in Aqueous Alkaline Solution. *J. Electrochem. Soc.* **2012**, *159*, H932−H944.
(43) Lyons, M. E. G.; Cakara, A.; O'Brien, P.; Godwin, I.; Doyle, R. L. Redox, pH sensing and Electrolytic Water Splitting Properties of Electrochemically Generated Nickel Hydroxide Thin Films in Aqueous Alkaline Solution. *Int. J. Electrochem. Sci.* **2012**, *7*, 11768−11795.
(44) Lyons, M. E. G.; Brandon, M. P. The Oxygen Evolution Reaction on Passive Oxide Covered Transition Metal Electrodes in Aqueous Alkaline Solution. Part 1-Nickel. *Int. J. Electrochem. Sci.* **2008**, *3*, 1386−1424.
(45) Kim, M.-S.; Hwang, T.-S.; Kim, K.-B. A Study of the Electrochemical Redox Behavior of Electrochemically Precipitated Nickel Hydroxides Using Electrochemical Quartz Crystal Microbalance. *J. Electrochem. Soc.* **1997**, *144*, 1537−1543.
(46) Wehrens-Dijksma, M.; Notten, P. H. L. Electrochemical Quartz Microbalance characterization of $Ni(OH)_2$-based thin film electrodes. *Electrochim. Acta* **2006**, *51*, 3609−3621.
(47) Bender, M. T.; Lam, Y. C.; Hammes-Schiffer, S.; Choi, K. S. Unraveling Two Pathways for Electrochemical Alcohol and Aldehyde Oxidation on NiOOH. *J. Am. Chem. Soc.* **2020**, *142*, 21538−21547.
(48) Su, X.; Wang, Y.; Zhou, J.; Gu, S.; Li, J.; Zhang, S. Operando Spectroscopic Identification of Active Sites in NiFe Prussian Blue Analogues as Electrocatalysts: Activation of Oxygen Atoms for Oxygen Evolution Reaction. *J. Am. Chem. Soc.* **2018**, *140*, 11286−11292.
(49) Görlin, M.; Ferreira de Araujo, J.; Schmies, H.; Bernsmeier, D.; Dresp, S.; Gliech, M.; Jusys, Z.; Chernev, P.; Kraehnert, R.; Dau, H.; Strasser, P. Tracking Catalyst Redox States and Reaction Dynamics in Ni-Fe Oxyhydroxide Oxygen Evolution Reaction Electrocatalysts: The Role of Catalyst Support and Electrolyte pH. *J. Am. Chem. Soc.* **2017**, *139*, 2070−2082.
(50) Ahn, H. S.; Bard, A. J. Surface Interrogation Scanning Electrochemical Microscopy of $Ni_{(1-x)}Fe_{(x)}OOH$ ($0 < x < 0.27$) Oxygen Evolving Catalyst: Kinetics of the "fast" Iron Sites. *J. Am. Chem. Soc.* **2016**, *138*, 313−8.
(51) Biesinger, M. C.; Payne, B. P.; Grosvenor, A. P.; Lau, L. W. M.; Gerson, A. R.; Smart, R. S. C. Resolving surface chemical states in XPS analysis of first row transition metals, oxides and hydroxides: Cr, Mn, Fe, Co and Ni. *Appl. Surf. Sci.* **2011**, *257*, 2717−2730.
(52) Grosvenor, A. P.; Biesinger, M. C.; Smart, R. S. C.; McIntyre, N. S. New interpretations of XPS spectra of nickel metal and oxides. *Surf. Sci.* **2006**, *600*, 1771−1779.
(53) Gong, M.; Li, Y.; Wang, H.; Liang, Y.; Wu, J. Z.; Zhou, J.; Wang, J.; Regier, T.; Wei, F.; Dai, H. An advanced Ni-Fe layered double hydroxide electrocatalyst for water oxidation. *J. Am. Chem. Soc.* **2013**, *135*, 8452−5.
(54) Bode, H.; Dehmelt, K.; Witte, J. Zur Kenntnis der Nickelhydroxidelektrode - I. Über das Nickel (II)-Hydroxidhydrat. *Electrochim. Acta* **1966**, *11*, 1079−1087.
(55) Klaus, S.; Cai, Y.; Louie, M. W.; Trotochaud, L.; Bell, A. T. Effects of Fe Electrolyte Impurities on $Ni(OH)_2$/NiOOH Structure and Oxygen Evolution Activity. *J. Phys. Chem. C* **2015**, *119*, 7243−7254.
(56) Faure, C.; Delmas, C.; Fouassier, M. Characterization of a turbostratic α-nickel hydroxide quantitatively obtained from an $NiSO_4$ solution. *J. Power Sources* **1991**, *35*, 279−290.
(57) Oesten, R.; Wohlfahrt-Mehrens, M.; Ströbele, S.; Kasper, M.; Huggins, R. A. Structural Aspects of Undoped and Doped Nickel Hydroxides. *Ionics* **1996**, *2*, 293−301.
(58) Delmas, C.; Braconnier, J. J.; Borthomieu, Y.; Hagenmuller, P. New Families of Cobalt Substituted Nickel Oxyhydroxides and Hydroxides Obtained by Soft Chemistry. *Mater. Res. Bull.* **1987**, *22*, 741−751.
(59) Mani, B.; Neufville, J. P. d. Dehydration of Chemically and Electrochemically Impregnated (Cl and El) Nickel Hydroxide Electrodes. *J. Electrochem. Soc.* **1988**, *135*, 800−803.
(60) Batchellor, A. S.; Boettcher, S. W. Pulse-Electrodeposited Ni−Fe (Oxy)hydroxide Oxygen Evolution Electrocatalysts with High Geometric and Intrinsic Activities at Large Mass Loadings. *ACS Catalysis* **2015**, *5*, 6680−6689.
(61) Hall, D. S.; Lockwood, D. J.; Bock, C.; MacDougall, B. R. Nickel hydroxides and related materials: a review of their structures, synthesis and properties. *Proc. R. Soc. A* **2015**, *471*, No. 20140792.
(62) Nørskov, J. K.; Rossmeisl, J.; Logadottir, A.; Lindqvist, L.; Kitchin, J. R.; Bligaard, T.; Jonsson, H. Origin of the Overpotential for Oxygen Reduction at a Fuel-Cell Cathode. *J. Phys. Chem. B* **2004**, *108*, 17886−17892.
(63) Diaz-Morales, O.; Ferrus-Suspedra, D.; Koper, M. T. M. The importance of nickel oxyhydroxide deprotonation on its activity towards electrochemical water oxidation. *Chem. Sci.* **2016**, *7*, 2639−2645.
(64) Govind Rajan, A.; Martirez, J. M. P.; Carter, E. A. Facet-Independent Oxygen Evolution Activity of Pure β-NiOOH: Different Chemistries Leading to Similar Overpotentials. *J. Am. Chem. Soc.* **2020**, *142*, 3600−3612.
(65) Tkalych, A. J.; Zhuang, H. L.; Carter, E. A. A. Density Functional + U Assessment of Oxygen Evolution Reaction Mechanisms on β-NiOOH. *ACS Catalysis* **2017**, *7*, 5329−5339.
(66) Jülich Supercomputing Centre. JUWELS: Modular Tier-0/1 Supercomputer at Jülich Supercomputing Centre. *J. Large-Scale Res. Facil.* **2019**, *5*, A135.

https://doi.org/10.1021/acsaem.1c03761
ACS Appl. Energy Mater. XXXX, XXX, XXX−XXX